The Astrophysical Journal, 893:137 (14pp), 2020 April 20 https://doi.org/10.3847/1538-4357/ab7b5c

Pointing Chandra toward the Extreme Ultraviolet Fluxes of Very Low Mass Stars

Jeremy J. Drake, Vinay L. Kashyap, Bradford J. Wargelin, and Scott J. Wolk
Smithsonian Astrophysical Observatory, 60 Garden Street, Cambridge, MA 02138, USA
Received 2019 January 6; revised 2020 February 17; accepted 2020 February 28; published 2020 April 23

Abstract

The X-ray and EUV emission of stars plays a key role in the loss and evolution of the atmospheres of their planets. The coronae of dwarf stars later than M6 appear to behave differently from those of earlier spectral types and are more X-ray dim and radio bright. Too faint to have been observed by the Extreme Ultraviolet Explorer, their EUV behavior is currently highly uncertain. We have devised a method to use the Chandra X-ray Observatory High Resolution Camera to provide a measure of EUV emission in the 50–170 Å range and applied it to the M6.5 dwarf LHS 248 in a pilot 10 ks exposure. Analysis with model spectra using simple, idealized coronal emission measure distributions inspired by the Chandra Low Energy Transmission Grating spectra of the M5.5 dwarf Proxima Cen and results from the literature finds the greatest consistency with a very shallow emission measure distribution slope, DEM $\propto T^{3/2}$ or shallower, in the range $\log T = 5.5$–6.5, although this could be an artifact of systematic errors. Instead, cooler, more solar-like differential emission measures (DEMs) with a wide range of slopes were able to match the observations. Within the limitations of systematic errors, model spectra constrained by this method can provide accurate (within a factor of 2–4) synthesis and extrapolation of EUV spectra for wavelengths <400–500 Å. At longer wavelengths, models are uncertain by an order of magnitude or more and depend on the details of the emission measure distribution at temperatures $\log T < 5.5$. The method is sensitive to the possible incompleteness of plasma radiative loss models in the 30–170 Å range for which reexamination would be warranted.

Unified Astronomy Thesaurus concepts: Late-type stars (909); Stellar activity (1580); X-ray stars (1823); Solar extreme ultraviolet emission (1493); Exoplanet atmospheres (487); Stellar coronae (305); M dwarf stars (982)

1. Introduction

Magnetic activity on stars like the Sun with outer convection zones is manifest through energetic photon and particle radiation in the form of UV–to–X-ray emission from hot coronal plasma and a hot magnetized wind. Both photon and particle emissions have a stochastic component where stored magnetic potential energy is more impulsively released in flares and coronal mass ejections. Magnetic activity is driven by stellar rotation and so gradually declines with time as stars lose angular momentum to stellar winds (e.g., Skumanich 1972; Wright et al. 2011; Garraffo et al. 2018). Understanding of the physics of stellar coronae remains incomplete, and its study continues to be a cottage industry in modern astrophysics.

The growing realization that planetary systems are extremely common around Sun-like stars has led to a resurgence in interest in stellar magnetic activity. Exoplanets have catalyzed a shift in focus from coronal physics itself to the effects of energetic stellar radiation on planetary atmospheres and environments. Both UV–X-ray emission and stellar winds are agents of atmospheric destruction. In our own solar system, the action of the solar wind stripped copious amounts of water from the atmosphere of Mars during the Noachian period about 4 Gyr ago (e.g., Jakosky et al. 2015). The roles of X-ray and EUV radiation in exoplanet atmospheric evaporation have been highlighted in several recent studies (e.g., Penz & Micela 2008; Murray-Clay et al. 2009; Sanz-Forcada et al. 2010; Owen & Jackson 2012; Owen & Wu 2013, 2016; Chadney et al. 2015), and there is now convincing evidence that planetary envelopes have been reduced and evaporated by the host star EUV and X-ray emission (e.g., Sanz-Forcada et al. 2011; Owen & Wu 2013). Planets that have received higher integrated doses of EUV and X-ray exposure tend to be smaller objects that appear to have lost part or all of their envelopes.

Based on a simplifying assumption that EUV and X-ray emission declines with time (due to stellar spin-down) at the same rate, Owen & Jackson (2012) found that X-rays dominate mass loss during early times when stellar activity is very high. At later times, EUV emission dominates. In their modeling, Owen & Jackson (2012) adopted the assumption of lockstep decline in EUV and X-ray fluxes because, in their words, "The evolution of the EUV luminosity is still observationally rather unclear." Current evidence seems to point to X-ray decline being more rapid than EUV decline (e.g., Sanz-Forcada et al. 2011; Chadney et al. 2015), but it is now apparent that a deeper understanding of how stellar EUV and X-ray fluxes relate to each other and change with time is key to understanding planetary atmospheric evolution.

The "Unobservable Extreme Ultraviolet" is a phrase coined some decades ago representing the largely mistaken belief that the interstellar medium (ISM) would be so opaque at EUV wavelengths that nothing could be observed. It is apt today because there is currently no facility capable of observing cosmic (i.e., nonsolar) EUV emission. While the longer wavelengths of the EUV bandpass (here loosely defined as 100–912 Å) are indeed essentially inaccessible for all but the most nearby stars, the Extreme Ultraviolet Explorer (EUVE) did accumulate the spectra of a number of either nearby or particularly active late-type stars in the 70–750 Å range (e.g., Drake 1996; Bowyer et al. 2000). These data have been used by different authors to examine the EUV flux and how it can be estimated using different proxies, such as X-ray flux (Sanz-Forcada et al. 2011) or Lyα emission (Linsky et al. 2014; Youngblood et al. 2016). However, these studies have been

limited to stars of spectral type M5 and earlier for the simple fact that later types were too faint for EUVE to observe.

The remarkable discoveries of Proxima b (Anglada-Escudé et al. 2016) and four additional planets around TRAPPIST-1, making a total of seven currently known (Gillon et al. 2017), has highlighted the case for M dwarfs being favorable candidate host stars with nearby Earth-like exoplanets amenable to detailed study. While M dwarfs are the most numerous stars in the Galaxy and will likely host the largest number of conveniently nearby exoplanets, their magnetic activity represents a proportionally larger fraction of their bolometric output than earlier-type stars, and longer spin-down timescales mean that this output stays higher for longer. Habitable zone planets around M dwarfs are then even more susceptible to EUV, X-ray, and stellar wind destruction.

The EUV flux from late-type stars originates from the chromosphere, transition region, and corona (e.g., Drake 1998; Linsky et al. 2014), and it is necessary to have an accurate description of all of these regions to understand the EUV radiative output of stars. Late-type M dwarfs (spectral types >M5) such as TRAPPIST-1 (M8 V) present a difficult case for the use of proxies to infer EUV radiation output. The effective temperature of an M8 dwarf is only about 2500 K, and its atmosphere is highly neutral. These stars are fully convective, and it has been conjectured that their dynamo activity is fundamentally different. Wright & Drake (2016) showed that fully convective stars down to type M5.5V do follow the same rotation–activity relation as earlier types. However, relative to bolometric luminosity both Hα ($L_{\rm H_\alpha}/L_{\rm bol}$) and X-ray ($L_X/L_{\rm bol}$) outputs are seen to decline toward later M spectral types (e.g., Mohanty & Basri 2003; Berger et al. 2010; Cook et al. 2014), while radio output tends to increase (e.g., Williams et al. 2014), with changes in behavior appearing to set in around spectral type M7–M8.

Since late M-type dwarfs do not appear to follow the same X-ray behavior as earlier types, we have no indication that their EUV fluxes do either, or how they behave at all. In the absence of an EUV observational capability, other observational and theoretical methods that are able to infer the EUV fluxes of late M dwarfs would be of considerable value. Peacock et al. (2019) developed theoretical atmospheric models that appear promising for constraining emission in the longer wavelengths of the EUV bandpass for very low mass stars. At shorter wavelengths, EUV emission stems from coronal temperatures $\log T \geqslant 5.5$. While X-ray observations can be used to develop coronal models for temperatures $\log T \geqslant 6$, there remains a gap in temperature coverage between a few 10^5 and 10^6 K that is crucial for constraining EUV fluxes.

Here we develop a method to utilize the Chandra X-ray Observatory High Resolution Camera spectroscopic detector (HRC-S) to provide EUV constraints. This detector has sensitivity well into the EUV range, out to 170 Å. We devise an observing method to utilize an off-axis region of the detector with a thinner Al coating that has higher sensitivity at wavelengths longward of 44 Å than the on-axis filter. We analyze a pilot observation of the late M dwarf LHS 248 and show that the observing method can provide quite tight observational constraints on its EUV flux in the 100–400 Å range. The target was chosen from the compilations of X-ray data for nearby low-mass M dwarfs by Cook et al. (2014) and Williams et al. (2014) and represents the brightest known example of a late M dwarf spectral type in X-rays feasible for observation, excluding Proxima Centauri. Proxima has been observed by the EUVE spectrometers and thus provides a valuable comparison.

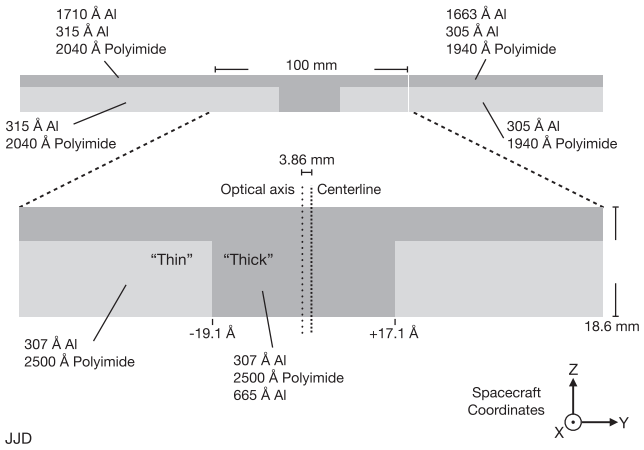

Figure 1. Schematic of the Chandra HRC-S UVIS with the center segment shown enlarged for detail. The filter characteristics of the thin and thick Al regions of the central segment referred to and used in the observations described here are noted. The observation of LHS 248 was obtained by pointing 5′.03 in the positive y direction so as to place the source at the thick/thin Al filter boundary to the right of center, as shown here.

The observing rationale is explained in Section 2. In Section 3 the various observations utilized in the study are described, and their analysis is related in Section 4. We discuss the issues involved in interpreting the data in Section 5 and reach our conclusions in Section 6.

2. EUV Sensitivity of the Chandra HRC-S

The Chandra X-ray Observatory (Weisskopf et al. 2003) Low Energy Transmission Grating (LETG)+HRC-S instrument reaches to wavelengths of 170 Å (and even longer with offset pointing), which is well into the EUV part of the spectrum. However, it is essentially a bright object spectrometer: depending on the intervening ISM absorption, spectra are spread over up to 300 mm of the microchannel plate detector, and for faint targets, the signal becomes background-dominated and swamped. With perhaps the exception of our second-nearest star, Proxima Cen (M6.5V; see Section 4.3.3), very late fully convective M dwarfs are generally beyond its reach.

A schematic of the HRC-S UV/Ion Shield (UVIS), designed to thwart optical and UV throughput and low-energy protons, is illustrated in Figure 1. The UVIS comprises three segments of Al-coated polyimide film. The two outer segments have the same characteristics within manufacturing tolerances, while the center segment is slightly different. Each filter segment covers a stack of microchannel plates and a charge readout grid connected to signal amplifiers that make up the rest of the detector.

The different segments were designed to handle the different wavelengths of the first-order dispersed LETG spectrum. Each has a strip of thicker Al coating serving as a "low-energy" suppression filter and designed for using primarily on the higher dispersed LETG orders throughput and a larger section of thinner Al as the main first-order detection region.

The center segment, together with the underlying microchannel plate detector, also serves as the backup imaging detector to the HRC-I, as well as being the prime Chandra

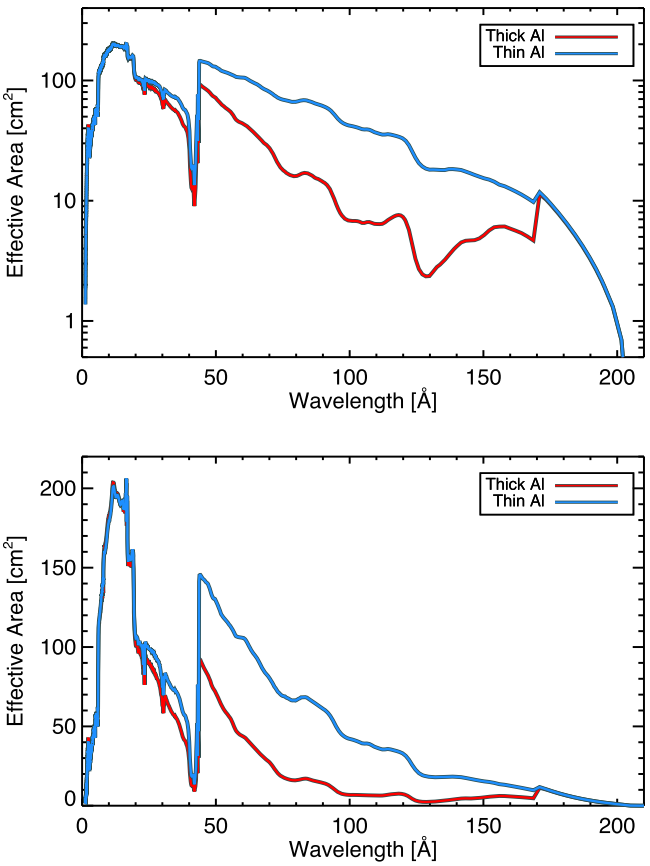

Figure 2. Effective areas of the Chandra HRC-S thin and thick Al filter regions computed at the location of the region boundary in the $-y$ direction from the detector center shown in logarithmic (top) and linear (bottom) units.

instrument for high timing resolution observations. Consequently, the region at the center where the aimpoint lies—the vertical part of the "T" shape in Figure 1—has a thicker Al coating for more aggressive UV and optical attenuation. Away from the detector center, during normal operation with the LETG in place, there is no signal from dispersed UV or optical photons, and the out-of-band rejection requirements are less stringent. Consequently, outside of the "T" region, the Al coating is much thinner. This filter region has significantly larger transmittance than the center region with the thicker Al coating.

The effective areas of the HRC-S "thin" and "thick" Al regions at the filter boundary in the $-y$ direction from the aimpoint were computed using the MKARF tool in the Chandra Interactive Analysis of Observations (CIAO) software package v4.9 and are illustrated in Figure 2. The Chandra HRC-S effective area is thought to be accurate to approximately 5% in absolute terms,[1] although this calibration is tied to the LETG dispersion; the off-axis angle of 5.′03 corresponds to a wavelength of approximately 17 Å (0.72 keV), and it is at that energy that the calibration is thought to be 5%. At widely different wavelengths, the calibration uncertainty will be somewhat larger. The uncertainty is almost all in the detector quantum efficiency, with the filter transmittance thought to be much more accurately calibrated through synchrotron measurement verification of a well-defined model (e.g., Meehan et al. 1997; Kraft et al. 2000). Thus, the relative effective areas for the two different filters should be at a level better than 5%.

The differences in the thick and thin effective areas become pronounced for wavelengths longer than the C K edge near 44 Å, up to the Al L edge near 170 Å, with the area being larger on the thin filter by typical factors of 2–4. It is this difference in effective areas that gives us some power to discriminate between shorter- and longer-wavelength emission.

3. Observations

The details of the Chandra observations of LHS 248 and Proxima Centauri analyzed in this study are listed in Table 1. All data reduction and computation of instrument response files followed standard procedures using the CIAO (Fruscione et al. 2006) software framework. Pertinent details for each are described further below.

3.1. LHS 248

Credible spectral types in the range M6 V (Davison et al. 2015) to M7.1 V (Terrien et al. 2015) have been assigned to LHS 248 (DX Cnc, GJ 1111), with the most common designation being M6.5 V (Alonso-Floriano et al. 2015). At a distance of 3.58 pc (Gaia Collaboration 2018), LHS 248 is the 18th-closest star (or star system) to the Sun. It is a rapid rotator and magnetically active flare star (e.g., Reiners & Basri 2007) with a period of 0.46 days (Morin et al. 2010; Newton et al. 2018) and is a probable member of the Castor moving group with an age of 200 Myr (Caballero 2010, and references therein). It was detected in a 16 ks ROSAT PSPC pointed observation with an X-ray luminosity of 4×10^{26} erg s^{-1} in the survey by Schmitt et al. (1995). The corresponding ratio between X-ray and bolometric luminosities is $\log L_X/L_{\rm bol} = -3.9$ (Cook et al. 2014), which is nearly a decade below the canonical saturation threshold of $\log L_X/L{\rm bol} \sim -3$ (see, e.g., Wright et al. 2011). Based on existing X-ray data, then, LHS 248 is the brightest, most feasible target for this EUV pilot study, excluding Proxima Centauri. The latter was observed using the EUVE spectrometers and provides a benchmark for comparison.

On 2018 May 22, LHS 248 was observed using the Chandra HRC-S for a net exposure of 10 ks. The target was acquired with an offset relative to the on-axis telescope aim point of +5.′03 in order to place the center of the telescope dither pattern on the boundary between the thick and thin Al filter regions.

An important aspect of the observation is that the filter resides above the detector surface by about 12 mm, and a point source at this height above the focal plane has a size of approximately 30″. The observation therefore employed a special 128″ × 16″ (full width) dither pattern that was enlarged relative to the standard 40″ × 40″ dither in the spacecraft Y-axis, along the long axis of the HRC-S, and compressed in the orthogonal spacecraft Z-axis.[2] This was done to minimize the time spent in transit over the thick/thin boundary and maximize the exposure when the source was entirely in either the thick or thin Al regions.

The basis of the observational method employing the spacecraft dither to sample the stellar emission on the different filters is that frequent sampling better accounts for source

[1] https://cxc.harvard.edu/cal/summary/Calibration_Status_Report.html

[2] Spacecraft Y- and Z-axes are aligned with "chip y" and "chip x," respectively, in HRC-S detector coordinates.

Table 1
Details of Chandra Observations Used in This Study

Target	ObsID	Instrument	t_{start}	t_{stop}	Exp. (s)
LHS 248	20165	HRC-S	2018 May 22 07:17:04	2018 May 22 10:30:12	10,065
Proxima	12360	HETG+ACIS-S	2010 Dec 13 00:19:15	2010 Dec 13 22:56:56	78,234
Proxima	19708	LETG+HRC-S	2017 May 31 16:25:42	2017 Jun 1 05:28:58	44,349
Proxima	20073	LETG+HRC-S	2017 May 15 23:29:05	2017 May 16 11:22:33	40,245
Proxima	20080	LETG+HRC-S	2017 May 18 09:21:04	2017 May 19 00:28:41	51,851
Proxima	20084	LETG+HRC-S	2017 Jun 3 04:45:24	2017 Jun 3 13:51:01	29,479

variability that can occur on the observation timescale than, for example, dividing the exposure time into two continuous pieces. Ideally, the dither period should be as short as possible. In practice, the shortest dither period achievable is limited by a maximum allowable spacecraft dither speed. In order to accommodate the longer *Y*-axis dither and not violate maximum spacecraft dither rates, the dither period in this axis had to be lengthened from the default 1087 to 2647 s. The dither pattern followed during the observation is illustrated in detector coordinates in Figure 3.

The sky image of the detected events is illustrated in Figure 4, together with the circular and annular regions used to extract the source and background signals, respectively. The source photons are spread over a distinctly larger detector area than for sources observed on-axis as a result of the degradation of the telescope point-spread function with increasing off-axis angle. The source extraction region has a radius of 5.″6, with the annular background region having an area 17.6 times larger.

3.2. Proxima Centauri

Proxima is an M5.5 dwarf with a mass of approximately 0.12 $M_{\odot}$ (Delfosse et al. 2000; Boyajian et al. 2012, and references therein) and a rotation period of about 83 days (Benedict et al. 1998; Kiraga & Stepien 2007; Savanov 2012; Suárez Mascareño et al. 2015). While of slightly earlier spectral type than LHS 248, its proximity has allowed for detailed study from infrared to X-ray wavelengths, and, despite its relatively slow rate of rotation, its activity level is not too dissimilar from the latter star. We use it here as a learning example to begin to understand the structure of the coronae of low-mass M dwarfs.

We use high-resolution Chandra observations of Proxima Centauri in the analysis described below in order to provide a simple test of our idealized emission measure distribution approach. Proxima was observed using the High Energy Transmission Grating (HETG; Canizares et al. 2000) and LETG (Brinkman et al. 2000) spectrometers in 2010 and 2017, respectively (see Table 1). The HETG observation used the Advanced CCD Imaging Spectrometer spectroscopic detector (ACIS-S), while the LETG observations employed the HRC-S.

4. Analysis

4.1. LHS 248 Light Curves

The source and background HRC-S light curves of LHS 248 binned at intervals of 200 s are illustrated in Figure 5, together with the times at which the source was on thick and thin Al filter regions. This latter calculation assumed that the source was a uniformly illuminated circle and had a radius of 15″ at the height of the UVIS above the detector. While the defocused source is likely to be slightly more donut-shaped than a uniformly illuminated circle, this will have only a second-order effect on the light-curve shape as the source crosses the thick/thin filter boundary and does not factor into the selection of intervals during which it lies entirely on either the thick or thin Al region.

At approximately 9000 s from the start of the observation, a large flare was observed in which the count rate was seen to rise by a factor of about 13 over the quiescent value. This is

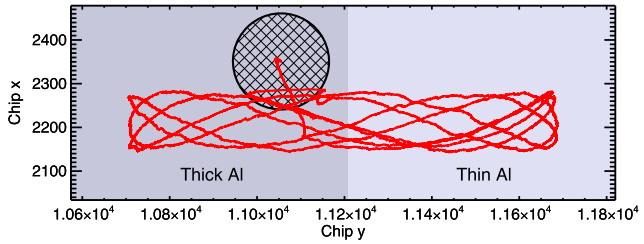

Figure 3. Dither pattern followed by LHS 248 in HRC-S detector coordinates. The hatched circle represents the size of the converging light cone at the height of the UVIS above the focal plane and is centered on the acquisition position of the target at the beginning of the observation. Note that the detector *Chip y* coordinate is oriented in the opposite direction to the spacecraft coordinates noted in Figure 1.

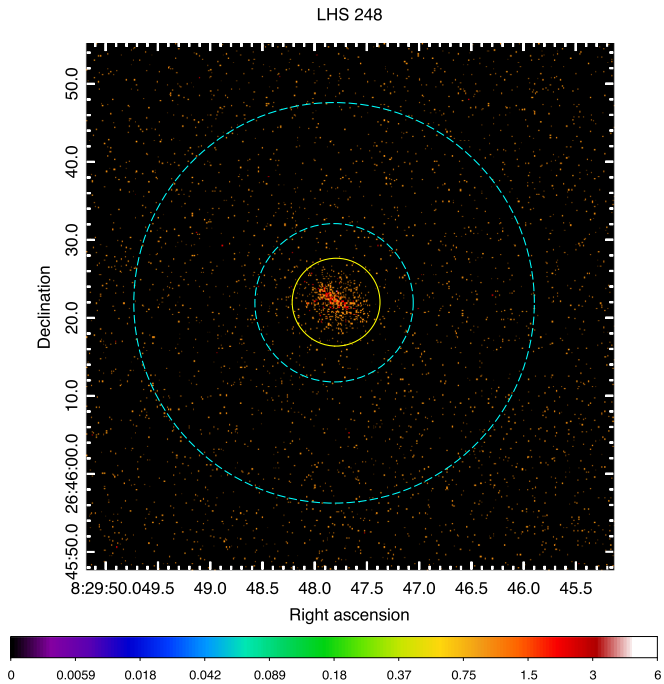

Figure 4. The HRC-S image of LHS 248 in sky coordinates illustrating the source and background signal extraction regions employed in the analysis. The asymmetric nature of the distribution of photon counts is a result of the source being observed off-axis.

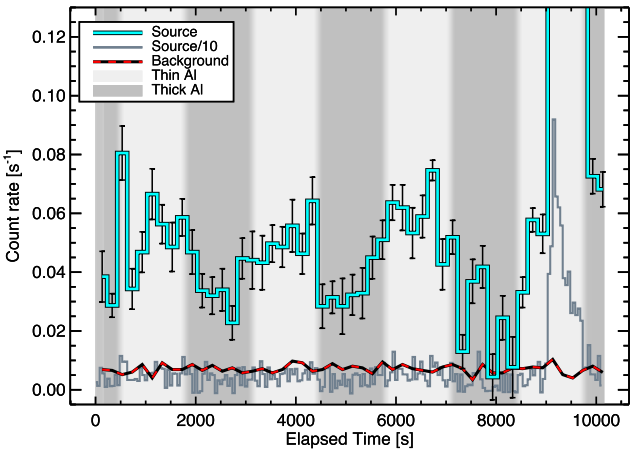

Figure 5. The HRC-S light curve of LHS 248 binned at 200 s intervals. Also shown are the background light curve with the same binning and the source count rate in 50 s bins divided by 10 to illustrate the flare that occurred about 9000 s into the observation. The shaded background represents the times at which the source was on thick or thin Al filter regions. The transitions between these regimes assumed that the defocused source could be represented by a uniformly illuminated circle with a radius of 15″.

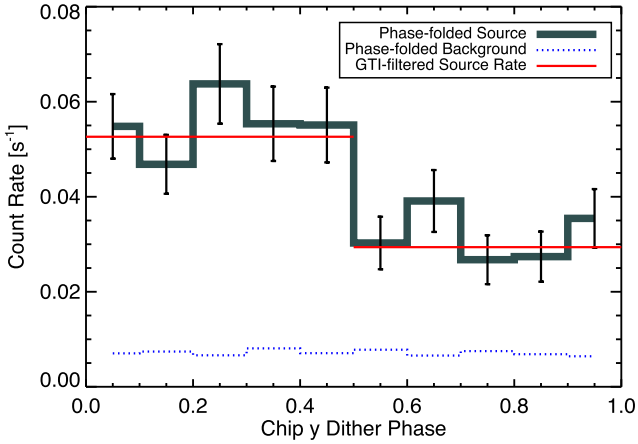

Figure 6. Source and background count rates as a function of the *Chip y* dither phase, excluding the large flare toward the end of the observation. The mean count rates for the exclusively thick or thin "good time intervals," for which the times when the source was crossing the thick/thin boundary have been filtered out, are also indicated.

brought out more clearly in Figure 5 in the light curve when binned at 50 s intervals and divided by a factor of 10. Since this flare occurred exclusively on the thin Al filter, we excluded it from the analysis described below.

Figure 5 demonstrates that, while the source was subject to some stochastic variability, the average count rate when on the thin Al filter was always larger than on the thick Al region, as expected.

The source and background light curves are shown as a function of the dither phase in Figure 6. The average source count rates over the whole observation, excluding the flare and time intervals during which the source was in transition between one filter region and the other—i.e., when source photons were simultaneously incident on both sides of the filter boundary—were 0.0294 ± 0.0031 (thick) and 0.0526 ± 0.0040 (thin), for a count rate ratio thin/thick $= 1.79 \pm 0.24$.

4.2. Assuming an Isothermal Coronal Plasma

The HRC-S detector has essentially no intrinsic energy resolution, such that the discrimination between EUV and X-ray photons can only be made by comparing the source count rates in the different filter regions. We proceed by employing optically thin plasma radiative loss models in order to, first, examine how the thick-to-thin filter count rate ratio is sensitive to the temperature and abundances in an idealized isothermal corona. In Section 4.4 we examine the extent to which different shapes of simple parameterized coronal emission measure distributions informed by available observations are consistent with the data. All of the calculations presented here were performed with the IDL[3]-based Package for INTeractive Analysis of Line Emission[4] (PINTofALE).

While both solar and stellar coronae are well known to comprise multithermal plasmas over a wide range of temperature, it is still useful to examine the extent to which the HRC-S thick and thin Al data are sensitive to isothermal plasma temperature and the assumed chemical abundance mixture. To this end, synthetic spectra were computed within PINTofALE for isothermal temperatures from 10^5 to 10^8 K using emissivities from the CHIANTI database version 7.1.5. We computed two sets of spectra: one for the solar abundances of Grevesse & Sauval (1998) and the other for an "inverse first ionization potential" (inverse FIP) chemical composition. The latter reflects the now-extensive observational evidence that in active stars, the abundance of elements with low FIP (<10 eV) appears to be depleted relative to elements with high FIP by factors of 2 or more. This is in contrast to the picture of lower-activity stars like the Sun, in which low-FIP elements appear to be enhanced (see, for example, Drake et al. 1997; Drake 2003; Laming 2015; Wood et al. 2018). These coronal abundance patterns also appear to depend on spectral type, with later K and M stars exhibiting a more inverse FIP pattern and earlier types tending toward a solar-like FIP effect (Wood et al. 2018).

An XMM-Newton study of four active mid-M dwarfs by Robrade & Schmitt (2005) found all to be characterized by an inverse FIP abundance pattern in which low-FIP elements such as Mg, Si, and Fe were depleted by about a factor of 2 relative to solar photospheric values, while high-FIP elements such as Ne, C, O, and N were relatively enhanced by up to a factor of 2. Robrade & Schmitt (2005) noted that the low FIP deficiency might simply reflect the stellar photospheric metallicity, leaving the high-FIP elements enhanced. For our inverse FIP abundance set, we adopted a simple pattern in which low-FIP element abundances were reduced by a factor of 2 relative to the Grevesse & Sauval (1998) mixture.

Synthetic spectra were convolved with the instrument effective area curves to obtain predicted count rates. We first investigated the effect of interstellar absorption for application to sources in general at arbitrary distances by computing the filter count rate ratios for a range of ISM absorbing columns from 10^{18} to 10^{22} cm^{-2}; ratios for lower column densities are essentially identical to that for 10^{18} cm^{-2}. The absorbing column toward LHS 248 is not known with any great degree of precision. According to the Local Interstellar Cloud model of Redfield & Linsky (2000),[5] the distance to the edge of the cloud in the line of sight toward LHS 248 is 2.3 pc. They

[3] Interactive Data Language ©Harris Geospatial Solutions.
[4] PINTofALE is freely available at http://hea-www.harvard.edu/PINTofALE/.
[5] http://lism.wesleyan.edu/cgi-bin/distlic.cgi

estimated an average neutral hydrogen density of 0.1 atoms cm^{-3} for a column density of 7.1×10^{17} cm^{-2}. Beyond the local cloud in the same sight line lies the Gemini cloud[6] (assuming that the structure of the local ISM region comprises discrete clouds; see, e.g., Redfield & Linsky 2015), although there is no strong constraint on its distance. Redfield & Linsky (2008) listed a distance of 6.7 pc to the closest star with measured absorption signatures from this cloud. It is therefore possible that there is no further significant absorption toward LHS 248 above that of the local cloud. A range of 5×10^{17}–3×10^{18} cm^{-2} should then comfortably bracket the actual neutral hydrogen column toward LHS 248.

The predicted count rate ratios for the filters as a function of isothermal plasma temperature for the different ISM absorbing columns, as well as for the solar and inverse FIP compositions for absorption appropriate to LHS 248, are illustrated in Figure 7.

4.3. Coronal Emission Measure Distributions of M Dwarfs

4.3.1. General Considerations

We base the analysis of LHS 248 below on simple parameterizations of the coronal emission measure distribution. In its most simple form, the emission measure as a function of temperature is usually expressed in the form of the differential emission measure (DEM) as a function of temperature, T,

$$\mathrm{DEM}(T) = n_e^2(T)\frac{dV(T)}{d\log T}. \quad (1)$$

Since the advent of high-resolution EUV and X-ray spectroscopy of, first, the solar corona and, subsequently, stellar coronae, many studies have examined the form of the plasma DEM. The reader is referred to the following work as a starting point for deeper exploration of the extant literature: Pottasch (1963), Withbroe (1975), Jordan (1976, 2000), Craig & Brown (1976), Bruner & McWhirter (1988), and Kashyap & Drake (1998) for solar work; and Drake et al. (1995), Sanz-Forcada et al. (2002, 2003), Huenemoerder et al. (2003), Telleschi et al. (2005), and Wood et al. (2018) for example stellar results.

The body of existing work demonstrates some universal aspects of the coronal DEM: from chromospheric temperatures of a few 10^4 K, the DEM decreases by approximately an order of magnitude to a minimum at temperatures of approximately $(1–4) \times 10^5$ K. The DEM then rises by approximately an order of magnitude or more to a maximum at temperatures between 10^6 and 10^7 K, beyond which it extends to higher temperatures over either a plateau or a shallow downward slope before a precipitate decline by several orders of magnitude. It is possible that there is further fine structure in the shape of the DEM in some cases, although assessing the veracity of such structure is far from trivial owing to the nature of the ill-constrained integral inversion problem of inferring the DEM from observed spectra (see, e.g., Craig & Brown 1976; Kashyap & Drake 1998).

4.3.2. The Case of Proxima: Chandra HETG Spectrum

While existing stellar DEM data exhibit common characteristics, there is essentially no detailed spectral information for late M dwarfs with which to verify that such characteristics do extend to the lowest-mass stars. Here we examine the Chandra HETG spectrum of Proxima Centauri in order to help establish the form of emission measure distribution to adopt for our target LHS 248. The analysis employed a parameter estimation approach in which the observed spectrum was fitted to a multithermal, optically thin plasma radiative loss model whose emission measure distribution at each temperature was allowed to vary.

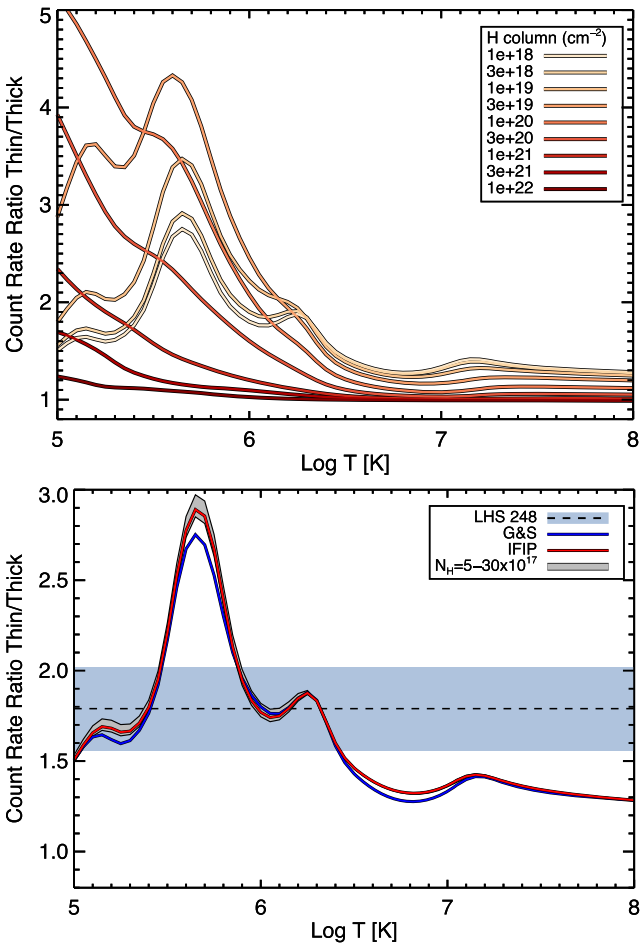

Figure 7. Predicted thin/thick filter count rate ratio for isothermal optically thin plasma radiative loss models. Top: solar (Grevesse & Sauval 1998) abundance mixture and different values of ISM neutral hydrogen column density. Bottom: column density range appropriate to LHS 248, including both solar ("G&S") and inverse FIP (see text) abundance mixtures; the observed ratio for LHS 248 is also indicated.

Proxima is the most well-known flare star in the sky, and in order to understand the context of the extracted spectra upon which our analysis is based, we first extracted the dispersed photon events in zeroth order to compute the X-ray light curve and assess flaring activity. An approximate correction for the effects of "pileup"—when photon events are lost or incorrectly counted due to multiple photon interactions at the same detector location during a single CCD frame—using pileup fraction estimates from the Portable, Interactive Multi-Mission Simulator[7] was made to the extracted light curve. The resulting corrected light curve is illustrated in Figure 8. Pileup fractions varied from a maximum of approximately 30% for the very peak of the flare at about 20 ks into the exposure to a minimum of about 2% for the lowest count rates and a more typical

[6] http://lism.wesleyan.edu/cgi-bin/dynlism.cgi

[7] http://cxc.harvard.edu/toolkit/pimms.jsp

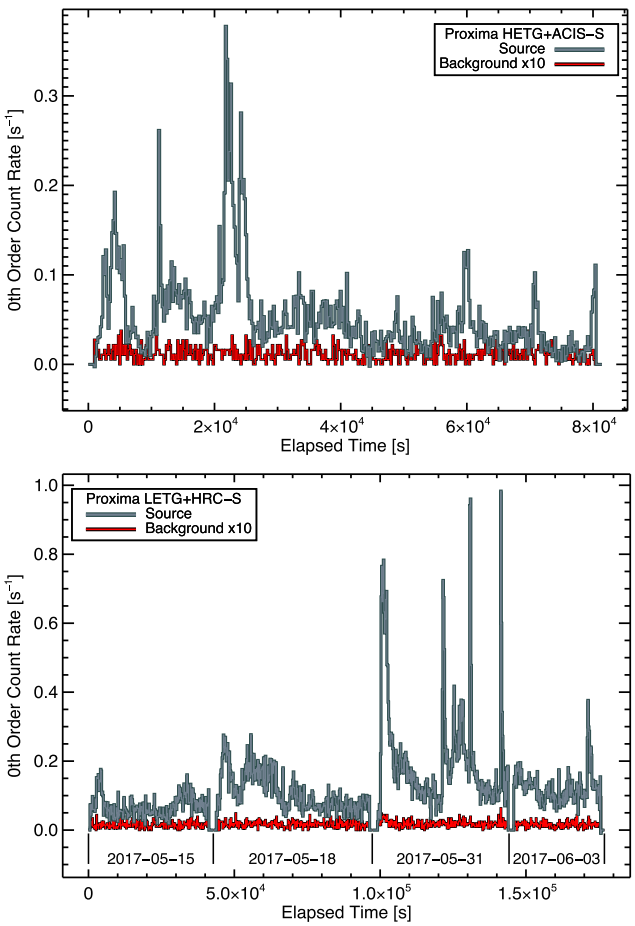

Figure 8. The X-ray light curves of Proxima observed with the Chandra HETG +ACIS-S (top) and LETG+HRC-S (bottom). Light curves were obtained from the zeroth orders in both cases and binned at intervals of 200 s. The HETG +ACIS-S zeroth-order light curve has been corrected for pileup (see text).

6% for count rates of $\sim$0.05 counts s^{-1}. The observation is characterized by a moderate, and likely typical, amount of flaring (see, e.g., the survey of Proxima X-ray observations by Wargelin et al. 2017), in which several events are observed to reach count rates an order of magnitude above the apparent quiescent rate.

Parameter estimation was undertaken using the *Sherpa* fitting engine within CIAO. Multiple Astrophysical Plasma Emission Code[8] thermal plasma models were adopted to represent the DEM on a fixed temperature grid, each with a common fixed abundance pattern whose absolute normalization —the metallicity—was free to vary. The temperature grid spanned the range $\log T = 6.25$–7.5 in intervals of 0.25, for a total of six thermal plasma components.

While the abundances could, in principle, be fitted simultaneously with the temperature structure, we found that the significantly larger number of free parameters required posed problems for the stability of the solution. The solar abundances of Grevesse & Sauval (1998), modified to approximate the inverse FIP pattern by increasing the abundances of C, N, O, Ne, and Ar by a factor of 2, as described in Section 4.2, were adopted.

Since the high-resolution Chandra spectra of Proxima comprise many bins with few counts, the Cash statistic (C_r; Cash 1979) was employed for minimization of model deviations from the data. This statistic is valid in the Poisson regime of low numbers of counts in which χ^2 approaches, relying on Gaussian uncertainties, are inapplicable. This allows the data to be analyzed without further grouping of neighboring bins and at full spectral resolution.

The HETG High Energy Grating (HEG) spectrum was fitted over the wavelength range 1.5–16 Å, while fits to the Medium Energy Grating (MEG) spectrum were restricted to 2–25 Å. Both HEG and MEG spectra were initially fit simultaneously, but the low signal-to-noise ratio (S/N) of the HEG spectrum led to difficulties in obtaining convergence, and the final adopted results were based on the best fit to the MEG spectrum. The best-fit model yielded a reduced statistic of 0.6 and a formal metallicity of $[M/H] = -0.37 \pm 0.04$, expressed in the conventional logarithmic bracket notation.

The best-fit model is shown superimposed on the MEG spectrum in the top panel of Figure 9, while the resulting emission measure distribution is shown in Figure 11.

4.3.3. Proxima Cen LETGS Spectrum

A global model fit of the Chandra Low Energy Transmission Grating Spectrometer (LETGS) spectrum similar to that performed for the HETG unfortunately proved infeasible due to the low S/N in the vast majority of the spectral bins. However, it was instead immediately instructive to simply superimpose the spectrum computed for the HETG best-fit parameters. This overlay is illustrated in Figure 9. Note that no scaling or adjustment to any parameters has been made, except to scale back the C and N abundances to their solar ratios, [C/Fe] = 0 and [N/Fe] = 0, for the illustrative reasons explained below. The agreement at wavelengths <25 Å is quite remarkable, indicating that the average activity level of the two observations, flares included, was essentially the same.

The coolest temperature constrained by the HETG data was an upper limit to the DEM at logarithmic temperature $\log T = 6.25$. The longer wavelengths of the LETGS spectral range (Figure 10) exhibit lines formed at cooler plasma temperatures than sampled in the HETG range, and we can, in principle, use these lines to better constrain the lower-temperature DEM. A glance at the top panel of Figure 10 reveals a slew of emission lines longward of 50 Å in the model spectrum that appear in generally good agreement with the observed spectrum in the sense that they at least do not exceed the observed flux.

We next illustrate two similar spectral models computed with cool extensions to the HETG DEM that are shown in Figure 11. The form of the DEM extension is fairly arbitrary but based on the generally observed trends noted in Section 4.3.1; we simply extrapolate from the trend in lower-temperature behavior seen here and found in M dwarfs by Robrade & Schmitt (2005; see Section 4.4 and Figure 11) using DEM $\propto T^{\alpha}$, with $\alpha = 3/2$ and 5/2. The spectrum corresponding to a shallower power-law slope, $\alpha = 3/2$, egregiously overpredicts several lines, most notably the O VI doublets at 104.8 and 150 Å and Ni X and XI at 148.6 and 148.4 Å, respectively. Instead, the spectrum corresponding to the steeper DEM slope, $\alpha = 5/2$, is in quite good agreement with the lines in the longer wavelengths of the LETG spectrum.

Returning to the elements C and N, whose abundances were not scaled to the inverse FIP pattern adopted for the HETG spectrum fitting for the spectra illustrated in Figure 9, we note

[8] http://www.atomdb.org/

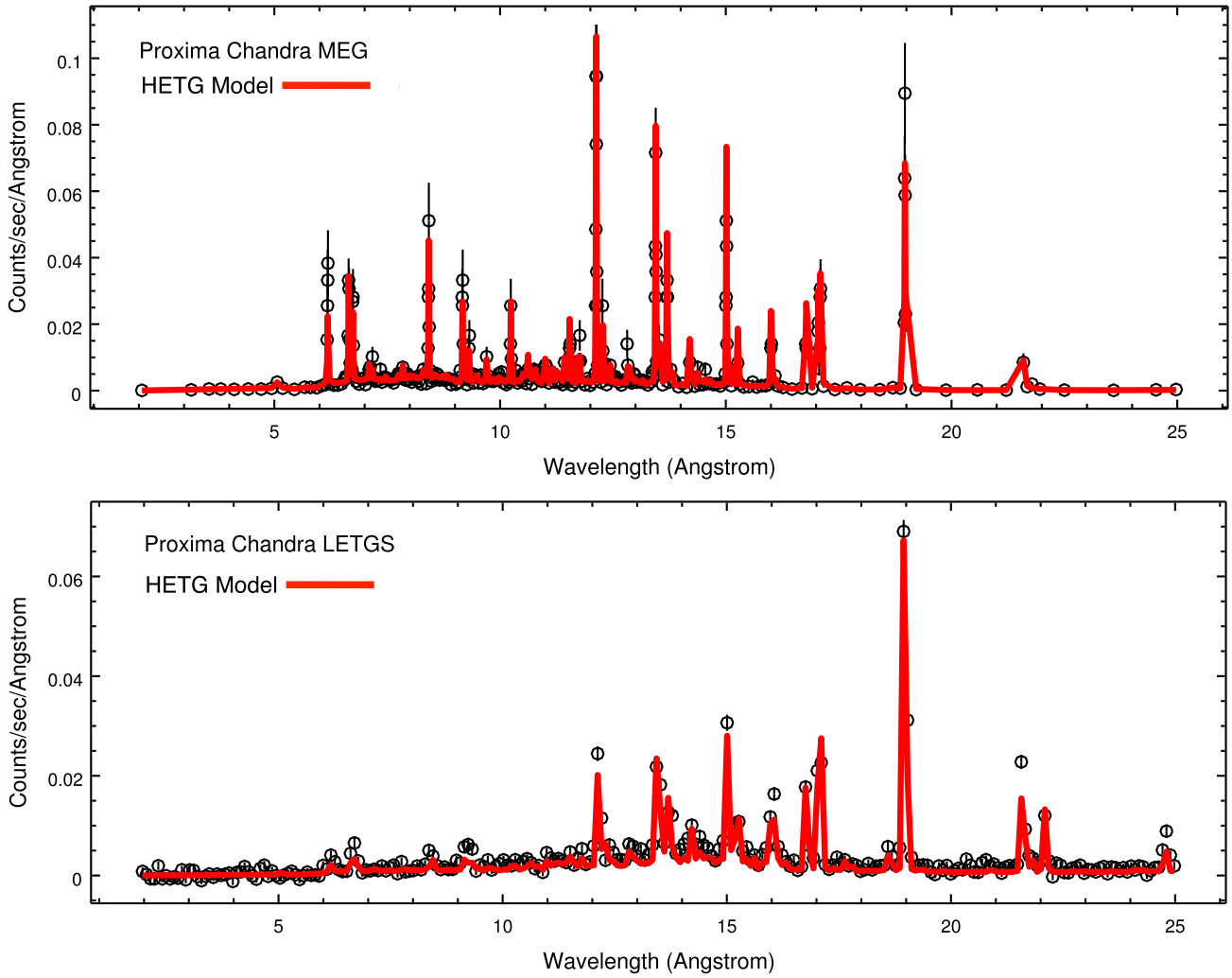

Figure 9. Chandra HETG (top panel) and LETG (bottom panel) spectra of Proxima overlaid with the best-fit HETG model spectrum (see text for details) in the 1–25 Å range.

that both of their H-like doublets at 33.7 and 24.8 Å denoted in Figure 10 are underpredicted by a factor of 2 in the $\alpha = 5.2$ spectrum. The He-like resonance lines at 28.8 and 40.3 Å are similarly underpredicted. This remains the case even for the elevated cool DEM $\alpha = 3.2$ spectrum, although to a slightly lesser extent. These lines are formed at (1–2) $\times$ 10^6 K, and their underprediction indicates that the inverse FIP abundance pattern extends to cooler temperatures than represented by the bulk of the HETG spectrum.

4.4. A Grid of Model DEMs for LHS 248

The general emission measure distribution shape that matches the Chandra HETG and LETG spectra of Proxima reasonably well comprises a fairly steep power-law slope from $\log T = 5.5$ until a peak at $\log T = 6.5$, a shallow power-law-like decline to $\log T = 7.25$, followed by a steep drop-off toward higher temperatures. By way of an interesting comparison to Proxima, Figure 11 also illustrates the average emission measure distribution for the four active mid-M dwarfs (AD Leo, EV Lac, AT Mic, and EQ Peg) whose XMM-Newton spectra were analyzed by Robrade & Schmitt (2005). The average of these M dwarf DEMs can be well approximated, at least within the temperature range probed by the XMM-Newton data, by two power-law components: a cool component rising toward the temperature of the peak emission measure and a declining power law toward higher temperatures.

Inspired by these similar-looking general DEM characteristics, and lacking detailed spectral information, we proceed to analyze the LHS 248 HRC-S photometry using a grid of model DEMs with a shape guided by the observed DEM characteristics. The general form adopted is

$$\begin{aligned}\Phi(T) &= \Phi(10^4\ \mathrm{K})\left(\frac{T}{10^4\ \mathrm{K}}\right)^{\alpha_T};\ 10^4 K \leqslant T \leqslant T_{\min}\\ &= \Phi(T_{\min})\left(\frac{T}{T_{\min}}\right)^{\alpha_{\mathrm{LC}}};\ T_{\min} \leqslant T \leqslant T_{\mathrm{peak}}\\ &= \Phi(T_{\mathrm{peak}})\left(\frac{T}{T_{\mathrm{peak}}}\right)^{\alpha_{\mathrm{UC}}};\ T_{\mathrm{peak}} \leqslant T \leqslant T_{\mathrm{sh}}\\ &= \Phi(T_{\mathrm{sh}})\left(\frac{T}{T_{\mathrm{sh}}}\right)^{\alpha_{\mathrm{HT}}};\ T_{\mathrm{sh}} \leqslant T \leqslant 10^8\ \mathrm{K}, \end{aligned} \quad (2)$$

where $T_{\min}$ is the temperature at which the DEM reaches a minimum, T_{peak} is the temperature at which the DEM peaks, T_{sh} is the maximum temperature reached by the DEM "plateau"

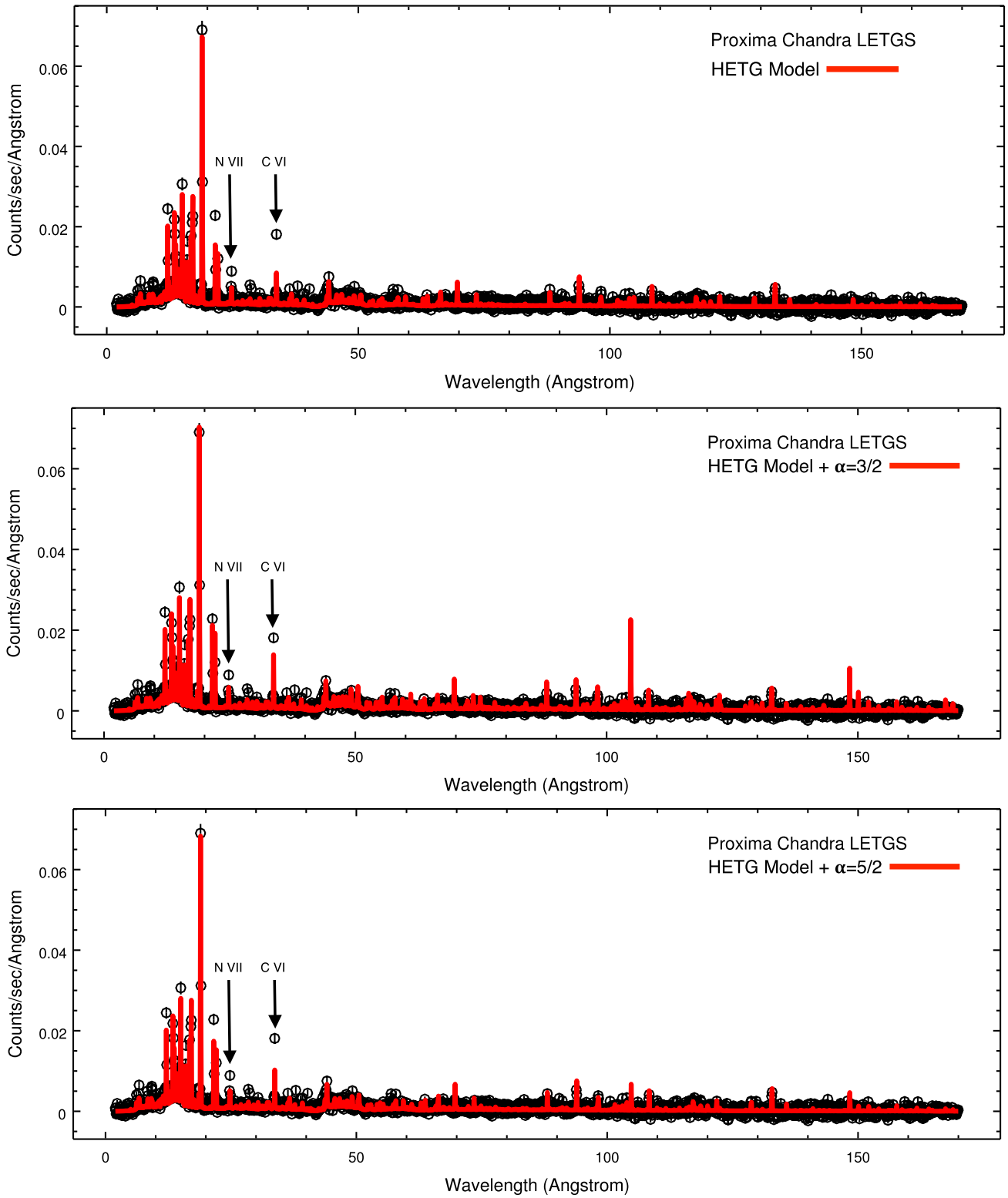

Figure 10. The LETG spectra of Proxima overlaid with the best-fit HETG model spectrum (see text for details) over the full range of the LETG+HRC-S showing the effect of changing the cool "tail" of the DEM. The first of these (top panel) illustrates the HETG model with no additional cool plasma components. The bottom two panels show the HETG model augmented by cool DEM extensions that follow the power-law relation DEM(T) $\propto T^{\alpha}$ with $\alpha = 3/2$ (middle panel) and $\alpha = 5/2$ (bottom panel). In order to aid the visualizations of the model comparisons, the spectra have been rebinned.

at its shoulder region, and α_T, $\alpha_{\rm LC}$, $\alpha_{\rm UC}$, and $\alpha_{\rm HT}$ are the power-law indices for the transition region, "lower corona," "upper corona," and high-temperature tail, describing the slopes to the DEM in the different temperature regions. The value of $\alpha_{\rm LC}$ is always positive, α_T and $\alpha_{\rm HT}$ are always negative, and $\alpha_{\rm UC}$ could, in principle, be either positive or negative but in our model DEMs takes on a fixed negative value.

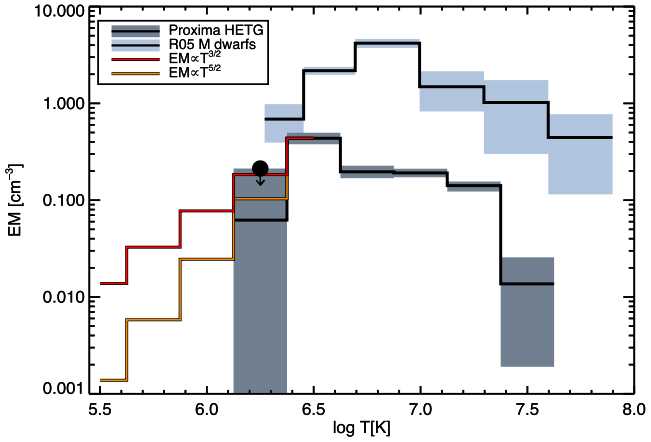

Figure 11. Emission measure distributions derived from HETG+ACIS-S observations of Proxima, together with the mean DEM from the XMM-Newton M dwarf study of Robrade & Schmitt (2005). The gray shaded regions represent uncertainties in the form of 90% confidence intervals. The cool extensions of the Proxima DEM tested on the LETG+HRC-S spectrum of Proxima are also illustrated.

In order to limit the number of parameters in the analysis to a manageable set, we use the observed DEMs in Figure 11 and appearing in the literature (Section 4.3.1) to constrain the general shape and parameter range to investigate. The temperature of the DEM minimum was assumed to be $\log T_{\rm min} = 5.5$, below which a fixed power law was assumed for all DEM models. Plasma at temperatures below $\log T = 5.5$ does not contribute significant emission in our HRC-S bandpasses in the presence of hotter coronal emission, and the details of this cooler part of the DEM are not important for our analysis. The full set of fixed constraints is

$$\begin{aligned} \log T_{\rm min} &= 5.5 \\ \log T_{\rm sh} - \log T_{\rm peak} &= 0.75 \\ \alpha_T &= -1.33 \\ \alpha_{\rm UC} &= -0.67 \\ \alpha_{\rm HT} &= -10. \end{aligned} \quad (3)$$

The parameters that were allowed to vary are the temperature of the peak DEM, $T_{\rm peak}$, and the amplitude of the DEM peak relative to the DEM at $T_{\rm min}$, specified by the scaling factor relating $\Phi(T_{\rm peak})$ and $\log\Phi(T_{\rm min})$. These relations are as follows:

$$\begin{aligned} 6.5 &\leqslant \log T_{\rm peak} \leqslant 6.9 \\ 0.4 &\leqslant \log \Phi(T_{\rm peak}) - \log \Phi(T_{\rm min}) \leqslant 3. \end{aligned} \quad (4)$$

The set of model DEMs investigated is illustrated in Figure 12. For each DEM, the synthetic spectrum was computed within the PINTofALE framework for the adopted inverse FIP abundance pattern, and the ratio of thick to thin filter count rates was calculated. The DEMs for which the count rate ratio was in agreement with the 1σ uncertainty of the measured value are highlighted. It is clear from the isothermal analysis illustrated in Figure 7 that cooler models than those described by Equation (4) are also likely to provide a good match to the observed filter ratio. We therefore also investigated a separate cool set in which the plateau was reduced to a logarithmic temperature width $\log T_{\rm sh} - \log T_{\rm peak} = 0.25$ and the peak temperature range explored was $6.1 \leqslant \log T_{\rm peak} \leqslant 6.5$. These DEMs are also illustrated in Figure 12.

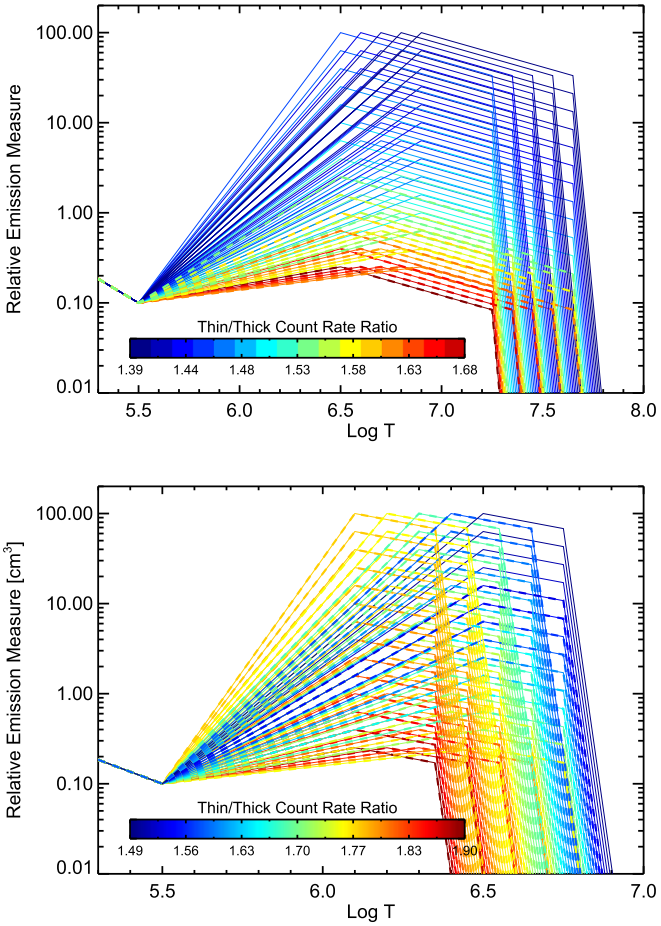

Figure 12. Idealized sets of DEMs investigated for LHS 248 in this study, color-coded according to their corresponding thin/thick predicted count rate ratios. Models that yielded a ratio in agreement with the observed value at the 1σ level are shown overlaid with bold dashed lines. The top panel shows models based on the observed DEMs for Proxima Cen and active mid-M dwarfs (Figure 11, Section 4.3.3). The bottom panel illustrates the cooler models that are almost all able to reproduce the observed count rate ratio within the statistical uncertainties.

5. Discussion

The off-axis pointing mode aimed at the HRC-S thick/thick Al filter boundary yielded photometric results for LHS 248 in agreement with general expectations: the count rate through the thin Al filter was found to be significantly larger than through the thick Al filter region owing to the larger effective area in the ∼40–170 Å range in the former. The analysis applied above suggests that this extra soft X-ray throughput is perhaps larger than might have been expected, since the observed ratio is ∼1.8 while ratios from our model DEM predictions top out below 1.7. There is one caveat to our discussion below. The implicit assumption in our approach is that the relatively high cadence switching between thick and thin filters eliminates significant systematic bias due to source variability and being brighter while in one filter compared with the other. This, of course, is an approximation whose propriety is difficult to assess, although, after excluding the flare, we do not expect this to be significantly larger than the statistical error on the count rate ratio. Further mitigation for source variability can be achieved simply by using a higher cadence—which unfortunately is not possible for Chandra—or longer observations with more filter cycles.

5.1. Isothermal Analysis

The isothermal analysis illustrated in Figure 7 suggests that the data are compatible with a rather cool corona with a temperature $\log T < 6.4$, quite similar to the dominant temperature of the solar corona. At face value, and based on the coronal activity versus rotation relations for early- to mid-M dwarfs, such a cool coronal temperature would be at odds with the rapid rotation of LHS 248 and its quite high X-ray luminosity in relation to its bolometric output, $L_X/L_{\rm bol} = -3.9$. However, we note that the coronal properties of late M dwarfs remain somewhat uncertain and still to be fleshed out in detail. In the presence of multithermal plasma, the simplistic isothermal interpretation of Figure 7 is of course not valid. An admixture of hotter and cooler plasma could also reproduce the observed count rate ratio.

The peak in the synthetic ratio at $\log T = 5.6$–5.7 indicates that plasma at that temperature has a particularly strong influence on the relative count rates in the different filters. This is largely due to the falloff in the short-wavelength end of the spectrum such that the dominant contribution to both filter count rates shifts longward of the C K edge. The flatter ratio for temperatures $\log T > 6.5$ is due to the opposite effect and increasing dominance of the spectrum at shorter wavelengths where the filter transmittances are similar. The influence of the abundance pattern—inverse FIP versus a solar photospheric mixture—makes little difference to the count rate ratio.

The small values of interstellar hydrogen column density toward the most nearby stars have a similarly weak influence. In general, the sensitivity of the filter ratio is expected to gradually diminish with increasing ISM absorption as the longer wavelengths of the spectrum are increasingly attenuated. However, the picture is complicated by strong lines of Fe IX–XI in the 170–200 Å range and longward of the Al L edge, where the two filter transmittances are very similar. Hence, the curves in the top panel of Figure 7 show quite a complicated pattern of predicted count rate ratio until the column densities reach about 10^{20} cm^{-2}, at which point further increases in column density yield the expected behavior.

We also note that the loci illustrated in Figure 7 could be affected by the "missing flux" in the plasma model that is discussed in Section 5.3.

5.2. How Steep Is the DEM?

The perhaps surprising result from the model DEM distribution analysis is that shallow DEM slopes based on the observed Proxima Cen and Robrade & Schmitt (2005) early-to-mid-M dwarf sample DEM shape are slightly more favored by the LHS 248 data. The thin/thick count rate ratio is illustrated for the model DEMs as a function of their power-law slopes from the emission measure minimum to the peak, $\alpha_{\rm LC}$ in our model notation, in Figure 13. Slopes of $\alpha_{\rm LC} \leqslant 3/2$ provide the best match to observations. It is clear that no model is strongly excluded, however, since all satisfy the observations within the 2σ limit (the observation analyzed here represents a pilot study; a longer exposure would have helped in providing more stringent constraints).

The cooler DEM models almost all fit the observed ratio; only the hottest of those with the steepest slopes fail at the 1σ level.

The value of the slope of the coronal emission measure has been examined in detail dating back to earlier solar studies.

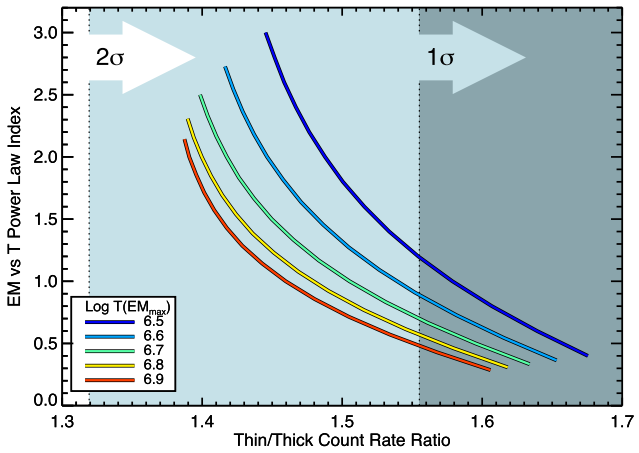

Figure 13. Loci of the DEM power-law index as a function of model thin/thick filter count rate ratio. The 1σ and 2σ lower limits to the observed ratio of 1.79 ± 0.24 for LHS 248 are indicated.

Those studies found values close to $\alpha_{\rm LC} = 3/2$ (e.g., Athay 1966; Jordan 1975, 1976), a result that can be understood in terms of the energy balance in spherically symmetric hydrostatic equilibrium and constant cross-section loop models considering the dissipation of heating within the corona and cooling through radiation and conduction back to the chromosphere. Extensive discussions have been provided by, e.g., Jordan (1976, 1980), Craig et al. (1978), Rosner et al. (1978), van den Oord et al. (1997), and, more recently, Jordan et al. (2012).

From a purely empirical perspective, the coronal emission measure distribution based on EUV lines observed in EUVE spectra is seen to steepen in more active stars, with values of $\alpha_{\rm LC} \sim 2$–4 having been derived (e.g., Laming et al. 1996; Laming & Drake 1999; Sanz-Forcada et al. 2003), similar to the cores of the brightest active regions on the Sun (Drake et al. 2000). The steeper slopes are possibly the result of flare rather than steady heating (e.g., Güdel 1997; Audard et al. 2000; Kashyap et al. 2002). Similar steeper slopes for active single and binary stars of a variety of spectral types were subsequently derived from X-ray observations with Chandra and XMM-Newton diffraction gratings (e.g., beginning with Drake et al. 2001; Huenemoerder et al. 2001, 2003, 2006; Telleschi et al. 2005). Based on these results, we would naively expect the DEM to be somewhat more steep than $\alpha_{\rm LC} \sim 3/2$. This expectation is, of course, predicated on extrapolation of the behavior of higher-mass stars to late M dwarfs.

The generally favored explanation for any changes in behavior going to the later spectral types is a speculated change in the underlying magnetic dynamo in fully convective stars and the form of the surface magnetic field that is produced, perhaps coupled with the effects of a very low electrical conductivity in the quasi-neutral atmospheres. Wright & Drake (2016) showed that there is no obvious change in X-ray behavior across the fully convective limit, with slowly rotating fully convective stars like Proxima and Barnard's Star adhering reasonably closely to the rotation–activity relation of stars with a central radiative zone. The results were further bolstered with a larger sample by Wright et al. (2018). The latest spectral type of the slow rotators in the Wright et al. (2018) sample is M6—comparable to the type at which the magnetic activity indicators appear to change in behavior.

Thus, the existing X-ray rotation studies do not provide any further strong clues as to the nature of the dynamo in the latest M types.

The different chromospheric and coronal behavior of very low mass stars compared with stars of mid-M spectral type and earlier was briefly referred to in Section 1. The fractional X-ray output, $L_X/L_{\rm bol}$, of the lowest-mass stars is systematically lower than for higher masses (e.g., Fleming et al. 2003) and exhibits a strong enhancement of the "supersaturation" effect—that X-ray output decreases with increasing rotation rate for the fastest rotators—and the scatter in X-ray output at a given rotation period is three times larger than for higher-mass stars (Cook et al. 2014). Chromospheric H_α fluxes are also relatively depressed (Delfosse et al. 1998; Fleming et al. 2003; Mohanty & Basri 2003). In contrast, the radio output of the lowest-mass stars is higher than expected based on the behavior of stars of higher mass (Berger 2006; Berger et al. 2008; Williams et al. 2014).

The characteristics of the X-ray emission itself of late M dwarfs is, however, not conspicuously different from their earlier counterparts, though there are indications of a possible decline in coronal temperature with later type. While Wheatley et al. (2017) found that the X-ray emission from the M8 dwarf TRAPPIST-1 could be approximated with a two-temperature optically thin plasma radiative loss model with temperatures of 0.15 and 0.83 keV, Fleming et al. (2003) found the temperature of the corona of the M8 dwarf VB 10 to be only 0.24 keV.

In summary, the DEM shape remains poorly constrained for late M spectral types, which was the main motivation for this pilot study. Simultaneous or contemporaneous observations in the X-ray range itself would provide the diagnostics to place a firm constraint on the hot coronal temperature and therefore narrow down the range of acceptable DEM models. We return to this in Section 5.4.

5.3. Missing Lines in the 30–170 Å Range?

Any interpretation of X-ray and EUV photometry in terms of plasma radiative loss models relies to some extent on the completeness of the model spectrum. There are indications that plasma models are still incomplete in the 30–170 Å range. This "missing lines" problem was first raised in the context of the analysis of EUVE spectra: global model fits to spectra in the 70–170 Å range found weaker line-to-continuum ratios than expected that were interpreted as either optical depth due to resonance scattering, low metal abundances, or very hot plasma that contributed only continuum to the region. The explanation is instead that flux in lines absent from the models was misinterpreted as continuum (see, e.g., the discussions in Drake 1996; Schmitt et al. 1996; Drake et al. 1997).

Before the launch of Chandra, the 30–70 Å spectral range covered by the LETGS had also been seldom observed, and models were relatively poorly tested in this region. Testa et al. (2012) used the Chandra LETGS spectrum of Procyon to evaluate atomic data relevant to the narrowband filters of the Solar Dynamics Observatory and concluded that the CHIANTI model (version 6) was missing flux amounting to up to a factor of 3 relative to the observed spectrum in some regions of the 50–130 Å range. Testa et al. (2012) noted that other databases shared the same problem. The culprit appeared to be some missing transitions from ions of abundant elements such as Ne, Mg, Si, S, and Ar with $n = 2$ ground states and Fe ions with $n = 3$ ground states (e.g., Jordan 1996; Lepson et al. 2005; Liang & Zhao 2010; Testa et al. 2012). These missing lines are more prominent in cooler coronal spectra; the DEM for Procyon peaks around $\log T \sim 6.3$, for example (e.g., Drake et al. 1995). The latter issue was mitigated in version 7.1 used here by the addition of a large number of configurations to atomic models of Fe VIII to XIV that produce flux in the 50–170 Å wavelength range (Landi et al. 2013).

Since any residual missing model flux is greater in the spectral region where the thin filter has a significantly larger effective area than the thick region, the effect would be to underestimate the thin/thick ratio for a given emission measure distribution. In order to compensate for this, the DEM would need to be shallower so as to have more cool plasma that can mimic the missing flux. It is possible, then, that the relatively shallow DEM slopes favored by the LHS 248 observation are partly an artifact of deficiencies in the radiative loss model.

5.4. Utility of the Thin/Thick Ratio for Predicting the EUV Flux

The ultimate goal of the experiment was to design an observation that would provide information to help assess coronal emission in the 100–900 Å EUV spectral range of stars that are too faint to be observed with the Chandra LETGS. To provide an illustration of the EUV leverage of our observations of LHS 248, the set of X-ray–EUV spectra predicted by both the Proxima-inspired DEM models with a temperature at DEM maximum of $\log T_{\rm peak} = 6.5$ and the solar-like cooler DEMs binned on 20 Å intervals (for other values of $T_{\rm peak}$ within the same confidence range, the spectra are very similar) are illustrated in Figure 14.

The EUV flux shortward of about 400 Å is dominated by temperatures $\log T > 5.5$, a regime for which our modeling approach should be able to provide an accurate description. Toward longer wavelengths, emission is dominated by cooler plasma, and our assumptions regarding the emission measure at its minimum, $\Phi(T_{\rm min})$, and at cooler temperatures, $\Phi(10^4\,{\rm K})$, begin to be important. Additionally, large contributors to the flux in the 800–900 and 450–500 Å ranges are the H Lyα and He I continua that are formed largely in the chromosphere and lower transition region (see also, e.g., Linsky et al. 2014). While our DEM models extend down to chromospheric temperatures, assumptions of optically thin, collision-dominated thermal equilibrium tend to break down there, and reproduction of the recombination continuum is not likely to be wholly accurate.

Proceeding with the assumption that the missing lines discussed in Section 5.3 do not have a significant impact on the photometric filter ratio interpretation (in any case, such an effect will be systematic in nature and will not affect the spread in model fluxes discussed here), Figure 14 demonstrates that, provided there are some constraints on the hotter part of the DEM, the general uncertainty in the flux at 100 Å within the 1σ range given by the spread in the model fluxes is only about 25%. Uncertainties grow, as would be expected, toward longer wavelengths. In the 200–300 Å region, the 1σ range is a factor of 2–3. The flux at 300 Å is dominated by the He II Lyα transition at 303.78 Å whose formation in the chromosphere, as for the H I and He I continua, is likely subject to complications from photoionization and recombination and thus might not be accurately represented by optically thin collision-dominated models in thermal equilibrium (e.g., Jordan et al. 1993, and references therein). The flux uncertainty grows to a factor of

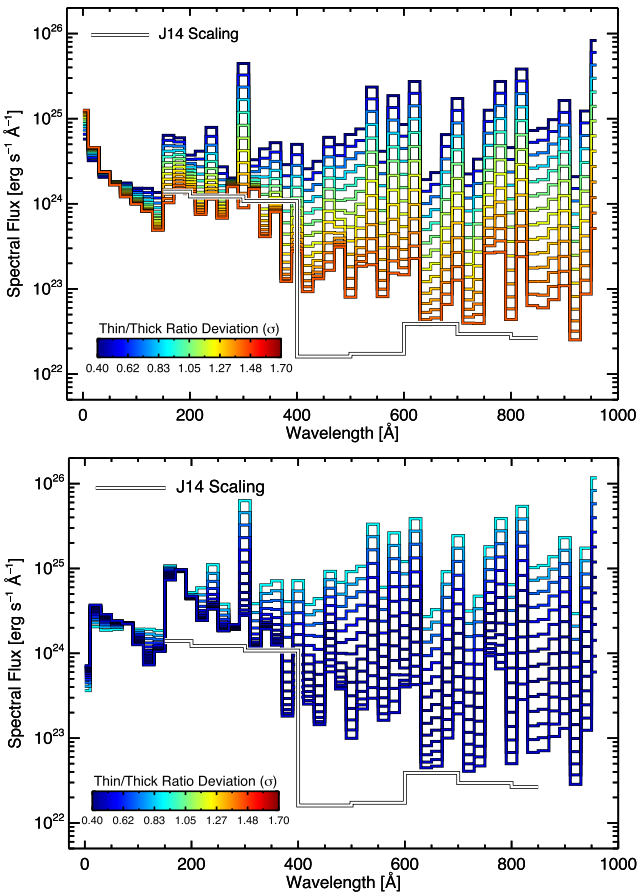

Figure 14. Synthetic spectra computed from the Proxima-based model DEMs with $\log T_{\rm peak} = 6.5$ (top) and cooler, more solar-like DEMs (bottom) for inverse FIP abundances binned on 20 Å intervals and color-coded according to the deviation in their predicted thin/thick filter ratios from the observed LHS 248 value. The flux predicted by the Linsky et al. (2014) empirical scaling based on the Lyα flux of Proxima, scaled to the radius of LHS 248, is also shown (denoted J14).

4–5 in the 300–400 Å range, and beyond that, it is about an order of magnitude.

These considerations lead us to conclude that the observational method developed in this paper can provide a reasonably accurate extrapolation of the EUV flux of stars. Given observations of higher S/N than attained for LHS 248, combined with contemporaneous X-ray observations to constrain the high-temperature emission measure as noted in Section 5.2, tight constraints on EUV emission in the 100–400 Å range are achievable. The efficacy of the filter ratio method is somewhat dependent on the completeness of radiative loss models; a reexamination of this issue would be strongly motivated.

Figure 14 also illustrates the EUV–Lyα scaling relations derived by Linsky et al. (2014) that are in common use. There appear to be no existing Lyα measurements for LHS 248, so we have simply scaled the flux for Proxima by the relative surface areas, $R_{248}/R_{\rm Prox}$, resulting in a flux of 4.3×10^{26} erg s^{-1}, to set the normalization. The agreement with our models shortward of 400 Å is good for the models with steeper DEM slopes. However, the scaling relations predict a strong discontinuity in the EUV flux at 400 Å by almost a factor of 100, in the sense that the flux in the 400–600 Å range appears to be strongly underpredicted. It can be seen from our spectral models that such a large discontinuity is unphysical in the sense that no superposition of plasma temperatures can conspire to give a spectrum with such a large jump in the flux at that wavelength. The minimum flux in the 400–600 Å range is given by purely hot coronal emission with temperatures in excess of 10^6 K that are adequately constrained by X-ray observations. Plasma at temperatures $<10^6$ K only adds to this.

6. Conclusions

A specially designed off-axis Chandra HRC-S observation of the late M dwarf LHS 248 succeeded in placing the source on the boundary between thin and thick Al coating regions of the UVIS filter. Dithering the source between the two regions of the filter resulted in a modulation of the observed count rate such that the rate for the thin filter was consistently higher than for the thick. The count rate difference is due to the effective area of the thin filter being larger by up to a factor of 4 than that of the thick filter in the 44–170 Å range.

A set of model DEMs based on the DEM shape found from an analysis of an archival Chandra HETG spectrum of Proxima and also guided by results in the literature was generated. These DEMs were used to compute model spectra that were assessed according to their ability to reproduce the observed thin/thick count rate ratio. Shallow power-law slopes to the DEM in the temperature range $5.5 \leqslant \log T \leqslant 6.5$ are favored at the 1σ level, but steeper slopes are accommodated within a 2σ range. It is possible that the shallow slopes are partially an artifact of incompleteness in current radiative loss models in the 30–170 Å range or a chance outcome of stochastic source variability leading to the source having been brighter when observed in the thin filter. Instead, DEM models with cooler, more solar-like temperatures yielded count rate ratios in good agreement with observations. Simultaneous X-ray observations would be required to distinguish between cooler and hotter coronal scenarios.

Regardless of the exact DEM model used, the modeling approach adopted here indicates that, in principle, Chandra HRC-S thin/thick photometric observations can provide an accurate—at least within a factor of 2–4—estimate of the EUV fluxes of stars in the 100–400 Å range. Constraints at longer wavelengths require more accurate knowledge of the cooler log $T < 5.5$ emission measure. We also find that the commonly used EUV scaling relations for the M dwarf spectral types of Linsky et al. (2014) have an unphysical discontinuity at 400 Å and likely underestimate the flux in the 400–600 Å range.

This work was funded by NASA Chandra grant GO8-19015X and NASA contract NAS8-03060 to the *Chandra X-ray Center*. J.J.D. thanks the director, Belinda Wilkes, for continuing advice and support.

Facility: Chandra X-ray Observatory.

Software: PINTofALE (Kashyap & Drake 2000), CIAO (Fruscione et al. 2006), CHIANTI (Dere et al. 1997; Landi et al. 2013).

ORCID iDs

Jeremy J. Drake https://orcid.org/0000-0002-0210-2276
Vinay L. Kashyap https://orcid.org/0000-0002-3869-7996
Bradford J. Wargelin https://orcid.org/0000-0002-2096-9586
Scott J. Wolk https://orcid.org/0000-0002-0826-9261

References

Alonso-Floriano, F. J., Morales, J. C., Caballero, J. A., et al. 2015, A&A, 577, A128
Anglada-Escudé, G., Amado, P. J., Barnes, J., et al. 2016, Natur, 536, 437
Athay, R. G. 1966, ApJ, 145, 784
Audard, M., Güdel, M., Drake, J. J., & Kashyap, V. L. 2000, ApJ, 541, 396
Benedict, G. F., McArthur, B., Nelan, E., et al. 1998, AJ, 116, 429
Berger, E. 2006, ApJ, 648, 629
Berger, E., Basri, G., Fleming, T. A., et al. 2010, ApJ, 709, 332
Berger, E., Basri, G., Gizis, J. E., et al. 2008, ApJ, 676, 1307
Bowyer, S., Drake, J. J., & Vennes, S. 2000, ARA&A, 38, 231
Boyajian, T. S., von Braun, K., van Belle, G., et al. 2012, ApJ, 757, 112
Brinkman, B. C., Gunsing, T., Kaastra, J. S., et al. 2000, Proc. SPIE, 4012, 81
Bruner, M. E., & McWhirter, R. W. P. 1988, ApJ, 326, 1002
Caballero, J. A. 2010, A&A, 514, A98
Canizares, C. R., Huenemoerder, D. P., Davis, D. S., et al. 2000, ApJL, 539, L41
Cash, W. 1979, ApJ, 228, 939
Chadney, J. M., Galand, M., Unruh, Y. C., Koskinen, T. T., & Sanz-Forcada, J. 2015, Icar, 250, 357
Cook, B. A., Williams, P. K. G., & Berger, E. 2014, ApJ, 785, 10
Craig, I. J. D., & Brown, J. C. 1976, A&A, 49, 239
Craig, I. J. D., McClymont, A. N., & Underwood, J. H. 1978, A&A, 70, 1
Davison, C. L., White, R. J., Henry, T. J., et al. 2015, AJ, 149, 106
Delfosse, X., Forveille, T., Perrier, C., & Mayor, M. 1998, A&A, 331, 581
Delfosse, X., Forveille, T., Ségransan, D., et al. 2000, A&A, 364, 217
Dere, K. P., Landi, E., Mason, H. E., Monsignori Fossi, B. C., & Young, P. R. 1997, A&AS, 125, 149
Drake, J. J. 1996, in ASP Conf. Ser. 109, Cool Stars, Stellar Systems, and the Sun, ed. R. Pallavicini & A. K. Dupree (San Francisco, CA: ASP), 203
Drake, J. J. 1998, ApJL, 496, L33
Drake, J. J. 2003, ApJ, 594, 496
Drake, J. J., Brickhouse, N. S., Kashyap, V., et al. 2001, ApJL, 548, L81
Drake, J. J., Laming, J. M., & Widing, K. G. 1995, ApJ, 443, 393
Drake, J. J., Laming, J. M., & Widing, K. G. 1997, ApJ, 478, 403
Drake, J. J., Peres, G., Orlando, S., Laming, J. M., & Maggio, A. 2000, ApJ, 545, 1074
Fleming, T. A., Giampapa, M. S., & Garza, D. 2003, ApJ, 594, 982
Fruscione, A., McDowell, J. C., Allen, G. E., et al. 2006, Proc. SPIE, 6270, 62701V
Gaia Collaboration, Brown, A. G. A., & Vallenari, A. 2018, A&A, 616, A1
Garraffo, C., Drake, J. J., Alvarado-Gomez, J. D., Moschou, S. P., & Cohen, O. 2018, ApJ, 868, 60
Gillon, M., Triaud, A. H. M. J., Demory, B.-O., et al. 2017, Natur, 542, 456
Grevesse, N., & Sauval, A. J. 1998, SSRv, 85, 161
Güdel, M. 1997, ApJL, 480, L121
Huenemoerder, D. P., Canizares, C. R., Drake, J. J., & Sanz-Forcada, J. 2003, ApJ, 595, 1131
Huenemoerder, D. P., Canizares, C. R., & Schulz, N. S. 2001, ApJ, 559, 1135
Huenemoerder, D. P., Testa, P., & Buzasi, D. L. 2006, ApJ, 650, 1119
Jakosky, B. M., Grebowsky, J. M., Luhmann, J. G., et al. 2015, Sci, 350, 0210
Jordan, C. 1975, in IAU Symp. 68, Solar Gamma-, X-, and EUV Radiation, ed. S. R. Kane (Dordrecht: D. Reidel), 109
Jordan, C. 1976, RSPTA, 281, 391
Jordan, C. 1980, A&A, 86, 355
Jordan, C. 1996, in IAU Coll. 152, Astrophysics in the Extreme Ultraviolet, ed. S. Bowyer & R. F. Malina (Dordrecht: Kluwer Academic), 81
Jordan, C. 2000, PPCF, 42, 415
Jordan, C., Ness, J. U., & Sim, S. A. 2012, MNRAS, 419, 2987
Jordan, S. D., Thompson, W. T., Thomas, R. J., & Neupert, W. M. 1993, ApJ, 406, 346
Kashyap, V., & Drake, J. J. 1998, ApJ, 503, 450
Kashyap, V., & Drake, J. J. 2000, BASI, 28, 475
Kashyap, V. L., Drake, J. J., Güdel, M., & Audard, M. 2002, ApJ, 580, 1118
Kiraga, M., & Stepien, K. 2007, AcA, 57, 149
Kraft, R. P., Chappell, J. H., Kenter, A. T., et al. 2000, Proc. SPIE, 4012, 493
Laming, J. M. 2015, LRSP, 12, 2
Laming, J. M., & Drake, J. J. 1999, ApJ, 516, 324
Laming, J. M., Drake, J. J., & Widing, K. G. 1996, ApJ, 462, 948
Landi, E., Young, P. R., Dere, K. P., Del Zanna, G., & Mason, H. E. 2013, ApJ, 763, 86
Lepson, J. K., Beiersdorfer, P., Behar, E., & Kahn, S. M. 2005, ApJ, 625, 1045
Liang, G. Y., & Zhao, G. 2010, MNRAS, 405, 1987
Linsky, J. L., Fontenla, J., & France, K. 2014, ApJ, 780, 61
Meehan, G. R., Murray, S. S., Zombeck, M. V., et al. 1997, Proc. SPIE, 3114, 74
Mohanty, S., & Basri, G. 2003, ApJ, 583, 451
Morin, J., Donati, J. F., Petit, P., et al. 2010, MNRAS, 407, 2269
Murray-Clay, R. A., Chiang, E. I., & Murray, N. 2009, ApJ, 693, 23
Newton, E. R., Mondrik, N., Irwin, J., Winters, J. G., & Charbonneau, D. 2018, AJ, 156, 217
Owen, J. E., & Jackson, A. P. 2012, MNRAS, 425, 2931
Owen, J. E., & Wu, Y. 2013, ApJ, 775, 105
Owen, J. E., & Wu, Y. 2016, ApJ, 817, 107
Peacock, S., Barman, T., Shkolnik, E. L., Hauschildt, P. H., & Baron, E. 2019, ApJ, 871, 235
Penz, T., & Micela, G. 2008, A&A, 479, 579
Pottasch, S. R. 1963, ApJ, 137, 945
Redfield, S., & Linsky, J. L. 2000, ApJ, 534, 825
Redfield, S., & Linsky, J. L. 2008, ApJ, 673, 283
Redfield, S., & Linsky, J. L. 2015, ApJ, 812, 125
Reiners, A., & Basri, G. 2007, ApJ, 656, 1121
Robrade, J., & Schmitt, J. H. M. M. 2005, A&A, 435, 1073
Rosner, R., Tucker, W. H., & Vaiana, G. S. 1978, ApJ, 220, 643
Sanz-Forcada, J., Brickhouse, N. S., & Dupree, A. K. 2002, ApJ, 570, 799
Sanz-Forcada, J., Brickhouse, N. S., & Dupree, A. K. 2003, ApJS, 145, 147
Sanz-Forcada, J., Micela, G., Ribas, I., et al. 2011, A&A, 532, A6
Sanz-Forcada, J., Ribas, I., Micela, G., et al. 2010, A&A, 511, L8
Savanov, I. S. 2012, ARep, 56, 716
Schmitt, J. H. M. M., Drake, J. J., Haisch, B. M., & Stern, R. A. 1996, ApJ, 467, 841
Schmitt, J. H. M. M., Fleming, T. A., & Giampapa, M. S. 1995, ApJ, 450, 392
Skumanich, A. 1972, ApJ, 171, 565
Suárez Mascareño, A., Rebolo, R., González Hernández, J. I., & Esposito, M. 2015, MNRAS, 452, 2745
Telleschi, A., Güdel, M., Briggs, K., et al. 2005, ApJ, 622, 653
Terrien, R. C., Mahadevan, S., Deshpande, R., & Bender, C. F. 2015, ApJS, 220, 16
Testa, P., Drake, J. J., & Landi, E. 2012, ApJ, 745, 111
van den Oord, G. H. J., Schrijver, C. J., Camphens, M., Mewe, R., & Kaastra, J. S. 1997, A&A, 326, 1090
Wargelin, B. J., Saar, S. H., Pojmański, G., Drake, J. J., & Kashyap, V. L. 2017, MNRAS, 464, 3281
Weisskopf, M. C., Aldcroft, T. L., Bautz, M., et al. 2003, ExA, 16, 1
Wheatley, P. J., Louden, T., Bourrier, V., Ehrenreich, D., & Gillon, M. 2017, MNRAS, 465, L74
Williams, P. K. G., Cook, B. A., & Berger, E. 2014, ApJ, 785, 9
Withbroe, G. L. 1975, SoPh, 45, 301
Wood, B. E., Laming, J. M., Warren, H. P., & Poppenhaeger, K. 2018, ApJ, 862, 66
Wright, N. J., & Drake, J. J. 2016, Natur, 535, 526
Wright, N. J., Drake, J. J., Mamajek, E. E., & Henry, G. W. 2011, ApJ, 743, 48
Wright, N. J., Newton, E. R., Williams, P. K. G., Drake, J. J., & Yadav, R. K. 2018, MNRAS, 479, 2351
Youngblood, A., France, K., Parke Loyd, R. O., et al. 2016, ApJ, 824, 101